Graph Machine Learning Framework for Gravimetry Data Analysis and Cavity Detection

Gourab Panda, Vipul Kumar Singh, Anil Kumar, Manabendra Saharia, and Sandeep Kumar

***Abstract*—Precise detection of small subsurface cavities is essential for geotechnical assessments, infrastructure stability, and resource exploration. Traditional gravity inversion methods have long been limited by poor resolution, noise-induced signal loss, and difficulties in capturing subtle, small-scale density variations. Conventional methods, such as damped least squares and regularization, typically require large amounts of high-quality data and treat sample points in isolation, which reduces their effectiveness in complex subsurface environments. To overcome these challenges, we introduce the Gravity Graph For Cavity (GGFC) framework—a novel, two-stage, graph-based semi-supervised learning approach that leverages advanced algorithms to accurately detect subsurface cavities even under realistic noise conditions. In the first stage, we construct a graph where the nodes represent cavities and the features represent anomaly points and cavity-induced density variations, with rich feature vectors capturing their spatial context and geometric properties. In the second stage, this graph is processed using state-of-the-art methods that integrate classical machine learning and deep learning techniques—specifically, Graph Neural Networks (GNNs) and Laplacian Regularized Least Squares (LapRLS)—to predict cavity depth and estimate radius by solving a graph-level regression problem. We further enhance our GNN approach to tackle complex geological structures by reframing cavity detection as a classification problem, marking a significant extension beyond traditional regression-based methods. Extensive experiments on synthetic datasets with limited labels and realistic noise conditions validate the robustness and versatility of our approach. Moreover, application to real-world datasets yields cavity depth and radius estimations that closely align with boring results, underscoring the framework's practical effectiveness.**

***Impact Statement*—Detecting micro-cavities beneath the Earth's surface is crucial for civil engineering, environmental science, archaeology, and disaster management. Accurate identification of subsurface voids can prevent structural failures, reduce sinkhole risks, and support sustainable development through informed land-use planning. However, recent methods often rely on extensive labelled datasets, which increase computational costs. The proposed graph-based semi-supervised method addresses this challenge by effectively capturing spatial and relational structures between cavity instances, even with minimal labelled data. It is also highly robust to noise, making it ideal for scenarios with limited resolution. This transformative approach is particularly valuable in geophysics, where low-resolution and noisy data are persistent obstacles. By leveraging graph-based frameworks, this method enables reliable and cost-effective cavity detection, contributing to safer infrastructure, the preservation of historic sites, and improved disaster resilience. The application aims to provide precise cavity specifications for projects involving small-scale cavities.**

Gourab Panda is with the Indian Institute of Technology, Delhi, India(e-mail: bsz218611@iitd.ac.in).

Vipul Kumar Singh is with the Indian Institute of Technology, Delhi, India.

Anil Kumar is with the Indian Institute of Technology, Delhi, India.

Manabendra Saharia is with the Indian Institute of Technology, Delhi, India.

Sandeep Kumar is with the Indian Institute of Technology, Delhi, India.

***Index Terms*—Cavity detection, Graph Machine Learning, Graph Neural Network, Gravity data, Laplacian Regularized Least Squares, Gravity Inversion**

I. Introduction

GRAVIMETRIC analysis measures changes in the Earth's gravitational field using sensitive gravimeters. This method helps explore underground structures by detecting density differences, offering valuable insights into what lies beneath the surface [1], [2]. Among its many applications, cavity detection [3] stands out due to its importance in civilian domains such as mining [4], [5], archaeology, geotechnical risk assessment, and environmental monitoring.

Cavity detection using gravity data is inherently an ill-posed inverse problem. Small anomalies produce subtle gravity variations that are easily obscured by noise, terrain effects, and instrument limitations [6]–[8]. Moreover, the problem often suffers from non-uniqueness, where multiple cavity configurations yield similar gravitational signatures [9]. Traditional approaches, such as parametric inversion techniques, struggle with robustness and accuracy, while data-hungry neural network models are brittle in low-data regimes and highly sensitive to noise. These limitations are exacerbated in field conditions, where accessibility and environmental variability pose additional constraints.

Recent advances in microgravimetry, including lightweight, high-precision gravimeters mounted on drones and field vehicles, make gravity surveys more accessible and scalable.

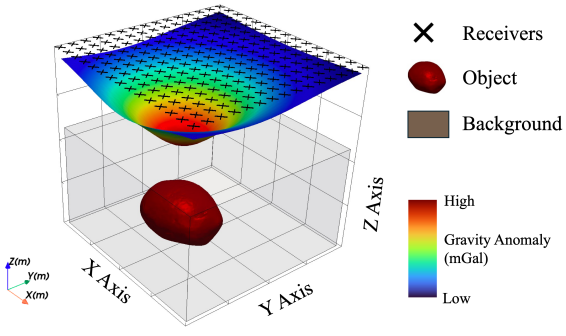

Fig. 1: Geophysical gravity anomaly representation. The top layer displays gravimeter readings as receivers (X marks) detecting subsurface density variations. The colour gradient indicates gravity anomalies in milligal (mGal) or microgal (μGal), reflecting density differences.

However, these advances demand equally agile and noise-resilient computational frameworks for interpreting the collected data. Existing methods [10], [11] often rely on image-based anomaly maps or black-box models, which overlook the spatial structure and relational patterns intrinsic to subsurface anomalies.

In this work, we present Gravity Graph for Cavity (GGFC), a graph-based machine learning framework that leverages spatial correlations among gravity measurements to robustly infer cavity parameters such as depth and radius. By representing gravimetric data as a graph, where each node encodes observation points, and edges encode spatial affinities between the cavities, we incorporate relational priors into the learning process. We propose two variants within this framework:

GGFC-LapRLS, which utilizes Laplacian Regularized Least Squares to enforce smoothness across spatially adjacent measurements, and GGFC-GNN, a Graph Neural Network that learns nonlinear mappings from gravity signals to cavity specifications by exploiting graph topology. Furthermore, we extend the analysis of the GGFC-GNN framework to address scenarios where anomalies deviate from regular shapes and exhibit irregular structures. In this analysis, we also consider both single-cavity and more than one cavity cases.

Our approach offers three key advantages: (i) improved prediction accuracy of cavity parameters even with sparse or noisy measurements, (ii) reduced dependence on large datasets, and (iii) robustness against measurement inconsistencies. We validate our methods using real-world gravimetric data from the Medford Cave site, demonstrating accurate recovery of both cylindrical and spherical cavity geometries.

By bridging the gap between classical inverse methods and modern graph-based learning, this work contributes a scalable, interpretable, and high precision tool for gravity based cavity detection. The proposed GGFC framework has the potential to enable automated, drone-based geophysical surveys for applications in civil engineering, mineral exploration, and beyond.

The paper is organized as follows: Section I introduces the inverse gravimetry problem. Section II reviews conventional and machine learning-based inversion methods. Section III outlines our methodology, including data generation and graph-based cavity modeling. Section IV describes the extension of the GGFC-GNN framework for irregular models. Section V presents the homophily analysis. Section VI discusses the experimental results and demonstrates the superiority of our approach. Section VII highlights the limitations of the proposed method, and Section VIII concludes the paper with key findings and final remarks.

II. Background and Related Work

Gravity surveys offer a non-intrusive method for detecting underground cavities, effective for both large-scale and localised investigations. Several studies have been conducted to explore the detection of cavities using gravimeters [12]–[16]. Void detection relies on density differences between cavities and surrounding rocks, creating anomalies measured in milligals or microgals [17]–[19]. A gravitational anomaly's cause is reproduced through a modeled approach, wherein a theoretical anomaly is calculated, and the model's shape is adjusted until the computed anomaly closely matches the observed anomaly [20]. Although the inverse problem is ill-posed, introducing further constraints on the shape and characteristics of the anomalous body helps minimize uncertainty [21]. Indirect methods use simple analytic equations for basic source objects like cubes, cylindrical, and spherical shapes [22].

Geophysical inverse problems are addressed using either conventional inversion or machine learning (ML) approaches. Conventional methods iteratively minimize data misfit based on physical models. Microgravity surveys provide a reliable method for cavity detection [23], but the inverse problem is inherently challenging and further complicated by the influence of noise [24]. Regularisation and additional constraints enhance stability and reduce uncertainty [25]. Li and Oldenburg [26] used the smooth inversion method for gravity data inversion. Fedi and Rapolla [27] performed inversion calculations to address the skin effect caused by the decreasing kernel function with depth. For highly nonlinear problems, conventional inversion methods struggle with depth resolution limitations and produce scattered results. One widely used inversion algorithm is the conjugate gradient method [28], [29]. There is a need for more nonlinear inversion algorithms.

The ML-based approach offers significant advantages for solving these problems [30]. Its flexibility and ability to adapt to complex and uncertain data make it well-suited for challenging scenarios. ML models can handle noise [31]. Eslam [14] previously utilized a deep neural network to estimate cavity specifications. In recent developments, Yang et al. [32] applied a U-Net CNN for spatial parameter prediction from gravity data. Yu-Feng et al. [33] proposed a 3D gravity inversion using a U-Net++ network. Huang et al. [34] employed a supervised deep fully CNN to generate a sparse subsurface density model distribution. He et al. [35] used a random-midpoint-displacement strategy to synthesize a realistic training dataset. Zhang et al. [36] introduced DecNet, a method that decomposes the 2D–3D inverse problem into a 2D–2D mapping process. Dong et al. [37] introduced a 3D gravity inversion based on the dual U-Net framework. Wang et al. [11] introduced the MS-UNets network for 3D gravity inversion, particularly in reconstructing subsurface density models like salt dome geometries.

Graph-based machine learning has diverse applications in geoscience. A graph with features is defined as $G = (V, E, W, X)$, where $V = \{v_1, v_2, \ldots, v_N\}$ is the set of N vertices, E is the set of edges, a subset of $V \times V$, and W is the adjacency (weight) matrix [38], [39]. A simple graph with non-negative weights $W_{ij} \geq 0$ is considered, without self-loops. The feature matrix is defined as $X = [x_1, x_2, \ldots, x_N]^\top$, where $X \in \mathbb{R}^{N \times d}$, and each feature vector $x_i \in \mathbb{R}^d$ is associated with a node of the graph G. The Laplacian (Θ) and adjacency matrix (A) are commonly used to represent graphs, with entries indicating connections between the vertices. A diagonal degree matrix D is defined, where $D_{ii} = \sum_j A_{ij}$ represents the degree of each node. Building on graph-based machine learning, a semi-supervised learning approach prop-

agates labels through a similarity graph, transferring label information from labeled to unlabeled data via strong network connections, leveraging the adjacency and degree matrices to model relationships within the graph [40]. Applications include analyzing water flow [41], predicting floods [42], studying climate patterns [43], identifying mineral deposits [5], and geospatial data fusion [44]. Recent advances in graph machine learning have shown promising results in various geoscience applications.

III. Proposed Framework

A. Proposed Formulation

Let $\mathbb{X}_i \in \mathbb{R}^d$ be the feature vector and $Y_i \in \mathbb{R}^m$ be the label vector corresponding to the i^{th} cavity, where, $i = 1, \ldots, n$ for a total of n cavities. A feature vector X_i represents gravity anomaly due to a cavity; the gravity anomaly is a function of the distance from the centre of the cavity and the density contrast between the cavity and the background. The corresponding label vector Y_i consists of the depth of the cavity center from the surface. Therefore, the problem under consideration is:

Given $n = l + u$ cavities and their parameters $X = (X_l, X_u)$ along with labels of only l number of cavities as Y_l, how can we predict the labels of the remaining u number of cavities Y_u?

Next, consider set $C_l = \{(X_i, Y_i)\}_{i=1}^{l} \in \mathcal{X} \times \mathcal{Y}$ and $C_u = \{(X_i)\}_{i=l+1}^{l+u} \in \mathcal{X}$, where $\mathcal{X}$ is the feature set and $\mathcal{Y}$ is the label, let the elements of the set C_l be sampled from probability distribution $\mathbb{P}$ over the ordered pair $\mathcal{X} \times \mathcal{Y}$. Samples of the domain set $X_i \in \mathcal{X}$ will follow the marginal distribution $\mathbb{P}_{\mathcal{X}}$ of $\mathbb{P}$. For the limited labelled data scenario, the goal of a learning algorithm is to estimate the conditional distribution $\mathbb{P}(Y|X)$ using both the labelled and unlabelled data as the training data. To incorporate the additional information of $\mathbb{P}_{\mathcal{X}}$ obtained because of the unlabelled data by capturing the intrinsic geometry of the marginal distribution through the graph of both unlabelled and labelled data, and performing label propagation and feature aggregation over the neighbourhood. The guiding principle is that if two data points from the domain set are close in the intrinsic distribution $\mathbb{P}_{\mathcal{X}}$, then the corresponding conditional distributions should be similar. For the cavity specification prediction, it means that given two cavities with similar features $X_i \sim X_j$ then the corresponding label vectors should also be similar $Y_i \sim Y_j$.

To build a learning framework based on the above guiding principle, these are the three main steps: i) Data generation, ii) Use of the feature space to obtain a geometric representation such that the samples having similar features are represented closer and connected, iii) Build a learning model such that geometric information be leveraged for learning the labels of unknown samples.

The cavity specifications or the labels Y_i are generally obtained using any known shape. So, synthetically generated data as labelled data X_l, Y_l and real data where we want to predict the cavity specifications as unlabelled data X_u, Y_u; therefore, $l < u$. Graph-based Semi-supervised learning attempts to address this by learning from both labelled as well as unlabelled data.

B. Synthetic Data Generation

The impact of gravity on the cavity may be calculated using geometrical models [45]. Assume the gravity effect is observed along the horizontal axis (x-axis);

TABLE I: Gravity anomaly equations for cylindrical and spherical cavity models.

Model	Gravity Anomaly
Cylindrical	$\Delta g(x) = \dfrac{200\pi G \Delta\rho R^2 D}{D^2 + \chi^2}$
Spherical	$\Delta g(x) = \dfrac{400\pi G \Delta\rho R^3 D}{3(D^2 + \chi^2)^{3/2}}$

TABLE II: Radius calculation formulas for cylindrical and spherical cavity models at cavity center ($\chi = 0$).

Model	Radius Formula
Cylindrical	$R = \left(\dfrac{\Delta g(x)\, D}{200\pi G\, \Delta\rho} \right)^{1/2}$
Spherical	$R = \left(\dfrac{3\, \Delta g(x)\, D^2}{400\pi G\, \Delta\rho} \right)^{1/3}$

Where G is the gravitational constant $6.67 \times 10^{-11} \frac{Nm^2}{Kg^2}$, $\Delta\rho$ is density contrast $(\frac{Kg}{m^3})$, R is the radius , D is the depth and χ is the measurement offset. The minima we got at $\chi = 0$ is called the cavity centre. By varying the offset value, we get anomalies at the surface. For the cavity detection problem, here we have two cavity specifications to determine, i.e., D and R. The units of gravimeter data are in milligals (mGal) or microgals (μGal). 1 gal is equal to 10^{-2} m/s^2. To enhance the model's robustness, small perturbations [46] were introduced into the synthetic data, ensuring more accurate predictions when applied to real-world datasets. This method helps bridge the gap between synthetic simulations and actual data, improving the model's performance and reliability in practical applications. $X = f(X + \epsilon)$; where $\epsilon \sim \mathcal{N}(0, \sigma^2 I)$ is a normal distribution with mean 0 and covariance $\sigma^2 I$.

C. Feature Vector from Gravity Anomaly

To apply the cylindrical and spherical cavity detection model as a graph machine-learning problem, we define a feature vector comprising anomalies Δg in particular directions and density contrast $\Delta\rho$. With the assumption that density contrast can be approximated for cavity detection problems, it can be used as a feature to improve the prediction of cavity specifications. For single cavity detection, varying offset values generate multiple anomaly points, creating a feature vector $[\Delta\rho, \Delta g_1, \Delta g_2, \ldots, \Delta g_{21}]^T$. The model is trained with depth D as the target. Once D is calculated, R is determined using Table II. This method requires input as graph data, where each node represents a feature vector corresponding to a cavity.

D. Gravity Graph For Cavity (GGFC)

The Gravity Graph For Cavity (GGFC) is a structured representation of cavities, where nodes correspond to a cavity, and

edges define spatial and feature-based relationships between them. This graph-based framework captures the geometric and physical interactions between cavities, aiding in the prediction of depth, and from depth subsequently radius using Table II. The construction of GGFC is based on two key principles: graph learning with K-Nearest Neighbors (KNN) and graph learning with the smoothness property.

Each node in the graph represents a distinct cavity, and connectivity is established using the KNN graph. In this approach, a vertex $v \in V$ is connected to its K most similar gravitational anomalies and the same density contrast. Each vertex is represented in a d-dimensional space, where the feature vector consists of anomaly points and the corresponding density contrast, such that $v \in \mathbb{R}^{d\times 1}$. The edges are weighted using the Gaussian Radial Basis Function (RBF) kernel [47]:

$$W_{ij} = \exp\left(-\frac{\|X_i - X_j\|^2}{2\sigma^2}\right) \tag{1}$$

where X_i and X_j are feature vectors corresponding to the i^{th} and j^{th} locations, respectively, and σ controls the similarity region. In our case, Gravimeter measurements are taken at 1-meter intervals along the X-axis, resulting in $d = 22$ (including density as a feature).

To enhance the graph structure, the smoothness property of graph signals is incorporated. The feature matrix is defined as: $X = [X_1, X_2, \ldots, X_n]^T$; where X_i represents the feature of the i^{th} cavity shape. The assumption is that features vary smoothly across connected nodes [48], meaning cavities with similar features should have a high edge weight. The smoothness is quantified using the Dirichlet energy:

$$\text{DE} = \frac{1}{2}\sum_{i,j} w_{ij}\,\|X_i - X_j\|^2 \tag{2}$$

A lower Dirichlet energy value indicates a smoother graph representation [48], [49]. The weighted adjacency matrix W is learned by minimizing Dirichlet energy while enforcing sparsity constraints:

$$w := \arg\min_{w\in\ w_m} \frac{1}{2}\sum_{i,j} w_{ij}\,\|X_i - X_j\|^2 - \alpha \mathbf{1}^\top \log(Sw) + \beta\|w\|_2^2 \tag{3}$$

where $\alpha > 0$ and $\beta \geq 0$ control graph connectivity and sparsity. The term $\|w\|_2^2$ ensures sparsity, while $\mathbf{1}^\top \log(Sw)$ enforces connectivity. S is the linear operator satisfying $Sw = W\mathbf{1}$. In this work, we have considered graph structures with positive weighted edges. This convex optimization problem is efficiently solvable [38], [48]. The final graph, constructed for cylindrical and spherical models, represents the spatial relationships between cavities.

E. Cavity Specification Prediction

The GGFC, as previously discussed, is further integrated with graph-based semi-supervised learning frameworks to predict cavity specifications such as depth and, therefore, radius.

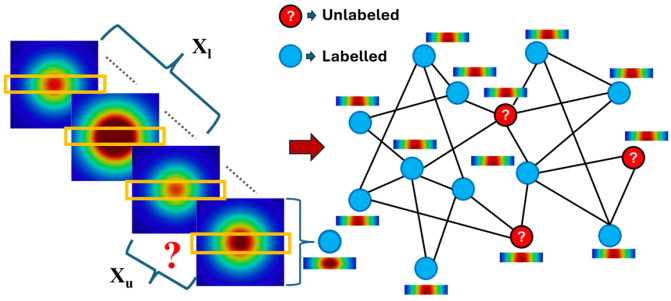

Fig. 2: GGFC: A graph-based model where each node represents a cavity. The features of each node include the gravity anomaly value at the center of the cavity and its density contrast.

Our model-agnostic framework seamlessly integrates with both traditional machine learning algorithms and deep learning models, enabling flexible and efficient cavity characterization.

1) Laplacian Regularized Least Squares (LapRLS): Cavity specifications, such as depth and radius, are influenced by gravitational anomalies and density distributions at various locations. Given l labelled cavity samples (x_i, y_i), where $i = 1, 2, ..., l$, and u unlabeled cavity (x_j), where $j = l+1, l+2, ..., l+u$, we define a Mercer kernel function $k(.,.)$ to capture spatial relationships between cavities. The LapRLS model [50] minimizes the following objective:

$$\min_{f\in\mathcal{H}} \frac{1}{l}\sum_{i=1}^{N}(y_i - f(x_i))^2 + \gamma_A\|f\|^2 + \frac{\gamma_B}{(u+l)^2} f^T L f \tag{4}$$

where $f = [f(x_1), f(x_2), ..., f(l+u)]^T$, and $L = D - W$ is the graph Laplacian, with W_{ij} representing spatial connectivity between cavity locations. The diagonal matrix D is given by $D_{ii} = \sum_j W_{ij}$. The hyperparameters γ_A and γ_B control the trade-off between fitting labeled cavity data and enforcing smoothness over the graph structure.

This formulation allows cavities with known depth labels to influence nearby unlabeled cavities, ensuring that depth estimation remains consistent with observed gravitational anomaly patterns.

2) Graph-Based Learning for Cavity Specification Prediction: After constructing the cavity graph, a Graph Neural Network (GNN) is employed to learn cavity representations by aggregating information from neighboring nodes. Through iterative message passing, the GNN captures spatial and structural relationships, allowing the model to refine predictions for unlabeled cavities based on the features of their labeled neighbors. Each node in the graph represents a cavity, with edges capturing spatial and feature-based relationships such as gravity anomalies and density contrast. The depth of an unlabeled cavity is predicted by aggregating information from its labeled neighbors.

Graph Convolutional Network (GCN): In GCN, cavity depth estimation is achieved by aggregating information from neighboring cavities [51]. Each node i represents a cavity, and $N(i)$ denotes its neighbouring cavities based on gravity

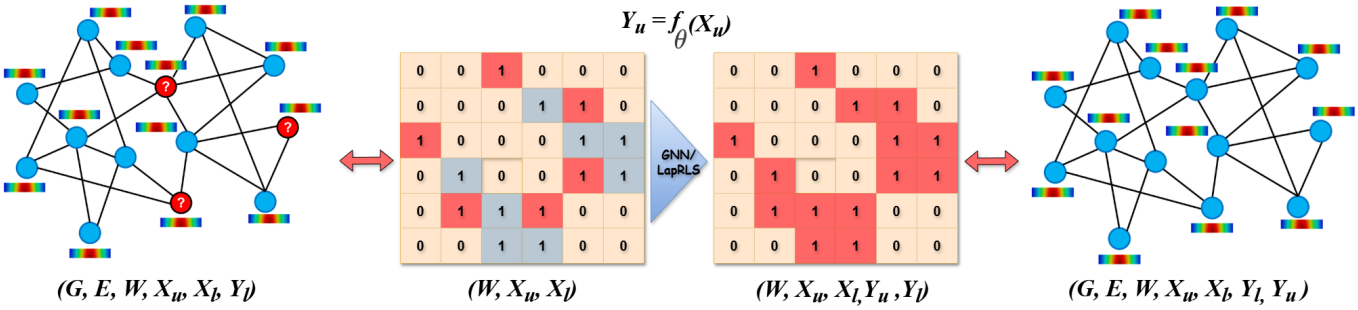

Fig. 3: GGFC framework: The input graph, consisting of both labelled and unlabeled nodes along with its adjacency matrix, is processed through the GNN/LapRLS framework. The updated adjacency matrix is then used to reconstruct the graph, enabling label prediction (depth) for unlabeled nodes.

TABLE III: GNN Architectures and Aggregation Mechanisms

Model	Aggregation Formula
GCN	$h_i^{(l+1)} = \sigma\left(b^{(l)} + \sum_{j\in N(i)} \frac{1}{c_{ij}} W^{(l)} h_j^{(l)}\right)$
GraphSAGE	$h_{N(i)}^{(l+1)} = \text{mean}\left(\{h_j^{(l)} : j \in N(i)\}\right)$ $h_i^{(l+1)} = \sigma\left(W \cdot \text{concat}(h_i^{(l)}, h_{N(i)}^{(l+1)}) + b^{(l)}\right)$ $h_i^{(l+1)} = \frac{h_i^{(l+1)}}{\|h_i^{(l+1)}\|_2}$
GAT	$e_{i,j}^{(l)} = a^T \text{concat}(W h_i^{(l)}, W h_j^{(l)})$ $\alpha_{i,j}^{(l)} = \text{softmax}_i\left(\text{LeakyReLU}(e_{i,j}^{(l)})\right)$ $h_i^{(l+1)} = \sigma\left(\sum_{j\in N(i)} \alpha_{i,j}^{(l)} W h_j^{(l)}\right)$

anomalies and density contrast. The cavity features $h_i^{(l+1)}$ are computed by summing the transformed features $h_j^{(l)}$ from neighboring cavities j, weighted by a learnable matrix $W^{(l)}$. The normalization factor c_{ij} ensures that highly connected cavities do not dominate the learning process. The bias term $b^{(l)}$ allows the network to capture additional variance in cavity, and the activation function $\sigma(.)$ (such as ReLU) introduces non-linearity, enabling better generalization in cavity depth prediction.

GraphSAGE: Instead of aggregating all neighbouring features like GCN, GraphSAGE samples and aggregates features from a subset of neighboring cavities, making it scalable for large datasets [52]. The representation of a cavity node is updated using both its own feature and a mean-pooling operation over its neighbors. The concatenation function in GraphSAGE combines the self-feature $h_i^{(l)}$ with the aggregated neighbor features $h_{N(i)}^{(l+1)}$. The weight matrices W_{self} and W_{neigh} control the influence of the cavity's own representation and its neighbors, respectively. Finally, L2 normalization ensures that feature magnitudes remain stable across layers. This learning approach allows the model to predict cavity specifications for unlabelled cavities.

Graph Attention Network (GAT): In GAT, rather than treating all neighboring cavities equally, the model assigns different importance levels to each neighbor through an attention mechanism [53]. The attention coefficient α_{ij} determines how much influence cavity j has on cavity i based on their feature similarity. This is computed using a learnable attention vector a and a concatenation operation, followed by a LeakyReLU activation function. The softmax function normalizes the attention scores across all neighbors. The final cavity representation $h_i^{(l+1)}$ is obtained as a weighted sum of neighboring cavity features, ensuring that cavities with stronger gravity anomalies and density contrast similarities exert a greater impact on depth prediction. This adaptive weighting mechanism makes GAT highly effective in cases where gravity anomalies and density contrast vary across different cavity formations, allowing the model to prioritize more relevant neighboring features for accurate depth estimation.

Each of these models provides a unique approach to propagating and refining cavity features. By leveraging these GNN architectures, cavity depth and radius predictions can be significantly improved by capturing complex spatial relationships within geological structures.

Based on these formulations, we propose a graph-based framework called Gravity Graph For Cavity (GGFC), illustrated in Figure 3.

3) GGFC-LapRLS: The GGFC-LapRLS algorithm follows a three-step approach. First, a dataset is created by assuming the cavity follows a known geometric shape, such as a cylinder or sphere, and generating synthetic anomaly points with density variations. This generated data is combined with real data to form a dataset $D \in \mathbb{R}^{n\times d}$. In the second step, a graph is constructed using GGFC with KNN-based graph learning, where l labelled samples $D \in \mathbb{R}^{l\times d}$ and u unlabeled samples $D \in \mathbb{R}^{(n-l)\times d}$ are incorporated, ensuring $n = l+u$. This graph representation captures structural variations within the dataset. In the final step, the Laplacian Regularized Least Squares (LapRLS) method is applied to predict cavity depth (D). The LapRLS algorithm leverages the graph structure to enforce smoothness in label predictions, ensuring that nearby samples in the graph have similar estimated labels, thereby improving prediction accuracy. Once the depth is estimated, the cavity radius (R) is computed using the equations in Table II. This approach integrates graph learning with semi-supervised regression for accurate cavity specification estimation.

4) GGFC-GNN: The GGFC-GNN algorithm also consists of three key stages. Initially, data is generated by assuming a predefined cavity shape (cylindrical or spherical) and introducing synthetic anomaly points with density variations. These are merged with real data to form a dataset $D \in \mathbb{R}^{n\times d}$.

In the second step, a graph is constructed using GGFC with Smooth Signal Learning, where both l labelled points $D \in \mathbb{R}^{l\times d}$ and u unlabeled points $D \in \mathbb{R}^{(n-l)\times d}$ are utilised, ensuring $n = l + u$. This graph representation helps in capturing complex relationships between the sampled points. A Graph Neural Network (GNN) is trained to predict cavity depth (D) at the node level, leveraging both node features and connectivity structure. The GNN aggregates information from neighbouring nodes through message passing, enabling effective generalization in a semi-supervised to infer cavity depth for unlabeled nodes. Once the depth (D) is estimated, the cavity radius (R) is computed using the corresponding equations in Table II. This deep learning-based approach enables robust and scalable predictions of cavity parameters, making it well-suited for complex and large-scale datasets.

Algorithm 1 GGFC-LapRLS: Depth Prediction

Input: Feature Matrix X_l, Label Matrix Y_l, kernel function k
Output: Depth: Y_u, and $f(x) = \sum_{i=1}^{l+u} \alpha_i k(x, x_i)$

1: Generate labeled data X_l, Y_l (Table I).
2: Combine real and synthetic data: $X_n = [X_l; X_u] \in \mathbb{R}^{n\times d}$
3: Construct a KNN graph on X_n; compute graph Laplacian $L \in \mathbb{R}^{n\times n}$
4: Compute kernel Gram matrix $K \in \mathbb{R}^{n\times n}$ using kernel $k(x_i, x_j)$
5: Define $Y \in \mathbb{R}^n$: $Y = [Y_l; \mathbf{0}_u]$
6: Define $J \in \mathbb{R}^{n\times n}$: $J = \text{diag}(\underbrace{1,\ldots,1}_{l}, \underbrace{0,\ldots,0}_{u})$
7: Solve for $\alpha^\star \in \mathbb{R}^n$:

$$\alpha^\star = \left(JK + \gamma_A lI + \frac{\gamma_B l}{n^2} LK\right)^{-1} Y$$

8: Return prediction function: $f(x) = \sum_{i=1}^{n} \alpha_i k(x, x_i)$

Algorithm 2 GGFC-GNN: Depth Prediction

Input: Feature matrix (X_l), Label matrix (Y_l)
Output: Depth (Y_u)

1: Generate labeled data X_l, Y_l (Table I).
2: Real data points X_u
3: Construct graph $G(V, E, W)$ using $X_l + X_u$ via smooth signal learning.
4: Compute node embeddings using GCN, GraphSAGE, or GAT (Table III).
5: Train GNN on (X_l, Y_l) and learned parameter θ
6: Predict $Y_u = F_\theta(X_u)$

Remark: *In our empirical evaluation, we have considered the problem in a transductive setting; however, GGFC-LapRLS can also be used for an inductive setting. We have developed gravity anomaly analysis methods leveraging graph-based frameworks in both traditional machine learning and deep learning paradigms. Experimental evaluations demonstrate that both frameworks exhibit competitive performance in gravimetry analysis. While the RLS method is outperformed by the GNN-based approach, the traditional framework, due to its significantly smaller parameter count, is better suited for deployment on portable or handheld devices and in drone-based monitoring systems.*

IV. Extension of GGFC-GNN for Irregular Models

In this section, we extend the GGFC-GNN framework to handle Irregular Models for both single and more than one cavity.

Gravity data involves calculating the gravity anomaly at the Earth's surface caused by a subsurface density distribution. Figure 4 provides a schematic overview of the prism-observation point configuration. Numerically, the process involves discretizing the subsurface into N rectangular prisms of density contrast ρ_j and observing gravity at M points on the Earth's surface.

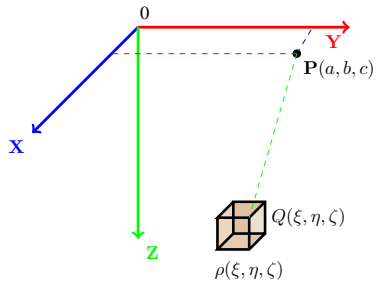

Fig. 4: Schematic representation of the relationship between an anomalous 3D rectangular prism and gravity measurement point $\mathbf{P}(a, b, c)$ at the surface.

The vertical anomaly, g_i at $P(a, b, c)$ due to prism is given by the analytical formula [54]:

$$g_i = -G\rho_j \sum_{p=1}^{2}\sum_{q=1}^{2}\sum_{s=1}^{2} \mu_{pqs}\Big[x_p \ln(y_q + r_{pqs}) + y_q \ln(x_p + r_{pqs}) - z_s \arctan\left(\frac{x_p y_q}{z_s r_{pqs}}\right)\Big]. \quad (5)$$

where G is the universal gravitational constant, $\mu_{pqs} = (-1)^{p+q+s}$ is the alternating sign for each prism corner, $x_p = a - \xi_p$, $y_q = b - \eta_q$, and $z_s = c - \zeta_s$ are the relative distances between the observation point $P(a, b, c)$ and the prism corner $Q(\xi_p, \eta_q, \zeta_s)$, and $r_{pqs} = \sqrt{x_p^2 + y_q^2 + z_s^2}$ is the distance between P and the corner Q. The coordinates (ξ_p, η_q, ζ_s) define the eight corners of the rectangular prism, where $\xi_p \in \{\xi_1, \xi_2\}$, $\eta_q \in \{\eta_1, \eta_2\}$, and $\zeta_s \in \{\zeta_1, \zeta_2\}$. This expression is evaluated over all eight corners of the prism, summing their contributions with the appropriate sign. The total gravity at a given observation point is obtained by summing the contributions from all prisms in the subsurface model.

A. Data Generation

In this study, we generate synthetic gravity anomaly data using a block model discretized into a 21×12 grid of rectangular prisms, as we consider 21 observation points along the surface and a depth of 12 m. Each prism represents a unit block of 1 m^3, with depth extending from the surface $z = 0$ m

to -12 m. Subsurface cavities are simulated by introducing clusters of blocks within the grid. Depending on the sample, these may form a single connected cluster or multiple clusters. Each cluster typically consists of 20–30 blocks, and cavity blocks are assigned a negative density contrast randomly sampled between -2500 and $-1500, \mathrm{kg/m}^3$. The vertical gravity anomaly at 21 evenly spaced surface stations is then computed using the analytical solution for rectangular prisms, and the overall response is obtained by summing contributions from all cavity blocks. Each dataset sample, therefore, contains the density contrast, the gravity response at all observation points, and the binary block labels that specify the cavity geometry, where (1) denotes a cavity and (0) denotes the background. This dataset includes samples with both single cavities and more than one cavity.

B. Loss Function.

We formulate the cavity detection problem as a binary classification task, where each block in the subsurface model is classified as either cavity (1) or background (0). To handle the strong imbalance between cavity blocks and the much larger background, we use the Dice Loss. For N training samples, with predicted probabilities $\hat{y}^{(i)} \in [0,1]^S$ and ground truth labels $y^{(i)} \in \{0,1\}^S$ (where S is the number of blocks per sample), the Dice coefficient for the i-th sample is

$$\mathrm{Dice}\big(y^{(i)}, \hat{y}^{(i)}\big) = \frac{2\sum_{j=1}^{S} y_j^{(i)} \hat{y}_j^{(i)}}{\sum_{j=1}^{S} y_j^{(i)} + \sum_{j=1}^{S} \hat{y}_j^{(i)}}. \tag{6}$$

The Dice Loss is then defined as

$$\mathcal{L}_{\mathrm{Dice}} = 1 - \frac{1}{N}\sum_{i=1}^{N} \mathrm{Dice}\big(y^{(i)}, \hat{y}^{(i)}\big). \tag{7}$$

This formulation directly maximizes the overlap between predicted cavity probabilities and true cavity locations, making it well-suited for the binary classification nature of the task and particularly effective in addressing the class imbalance inherent in gravity inversion problems.

V. Homophily analysis

Homophily in graphs is typically defined based on similarity between connected node pairs, where two nodes are considered similar if they share a similar node label. Homophily ratio is defined based on [55]. While there exist multiple metrics to quantify homophily, e.g, the label smoothness defined in [56] or the network assortativity in [57]. We adopt assortativity as it is easily generalised to nodes and edges.

Definition 1: Label-Based Homophily

Given a graph $G(V, E)$ and a node label vector y, the edge homophily ratio quantifies how often connected nodes share the same label. Formally:

$$h\left(G, \{y_i; i \in V\}\right) = \frac{1}{|E|} \sum_{(j,k)\in E} \mathbb{1}\left(y_j \sim y_k\right) \tag{8}$$

where $|E|$ is the total number of edges in the graph and $\mathbb{1}$ is the indicator function that returns 1 when the labels are similar and 0 otherwise. This metric captures the global proportion of label-consistent edges and is widely used to assess the suitability of a graph for label-based tasks such as node classification. Graphs with $h(\cdot)$ close to 1 are considered highly homophilous, which typically supports better performance in learning tasks that rely on neighbourhood consistency (typically, $0.5 \leq h(.) \leq 1$).

Definition 1.1: Global Node Label Assortativity

Global assortativity captures the overall structural tendency of nodes with similar labels to be connected across the entire graph. It serves as a correlation coefficient between node label similarity and network connectivity, providing a single scalar that reflects global homophily:

$$r_n^{\text{global}} = \frac{\sum_i e_{ii} - \sum_i a_i b_i}{1 - \sum_i a_i b_i} \tag{9}$$

where e_{ij} denotes the fraction of edges connecting nodes of type i and j, and $a_i = \sum_j e_{ij}$, $b_j = \sum_i e_{ij}$ represent the marginal distributions. A value of $r_n^{\text{global}} \to 1$ indicates strong global homophily, while values near 0 suggest random mixing. This measure complements the edge homophily score by accounting for distributional imbalance in label frequencies and edge patterns. In practice, higher global assortativity often correlates with improved classification accuracy, as label information tends to be more coherently clustered [57], [58].

Definition 1.2: Local Node Label Assortativity

Local assortativity focuses on individual nodes and evaluates the label agreement within their immediate (1-hop) neighborhood. It enables more fine-grained analysis of local label consistency, revealing structural or semantic variations that global metrics might miss. It is defined as:

$$r_n^{\text{local}}(u) = \frac{|\{v : v \in N(u) \wedge y_u \sim y_v\}|}{|N(u)|} \quad ; \quad u \in V \tag{10}$$

where $N(u)$ denotes the 1-hop neighbors of node u. High local assortativity values indicate that a node is surrounded by similarly labeled nodes, which typically benefits local aggregation-based models like GCNs. By examining local consistency, this metric helps identify heterogeneous regions of the graph and may guide neighbourhood-aware model design or preprocessing [57], [58].

Together, these measures offer complementary perspectives on how label information aligns with graph structure. In our experiments, we observe that graphs with higher global and local homophily measures tend to support better downstream classification performance, particularly for methods that rely on neighborhood similarity or smoothness assumptions.

In graph-based models, we aim to learn a weighted adjacency graph that accurately represents the underlying data distribution $\mathbb{P}_{\mathcal{X}}$. A key principle in constructing such a graph is homophily, which states that similar data points in the feature space should have similar attributes or labels. Graph-based semi-supervised learning utilizes homophily to infer missing label information. If two data points, X_i and X_j, are close in the intrinsic distribution $\mathbb{P}_{\mathcal{X}}$ (i.e., they share similar features), their conditional distributions should be similar. Consequently, the label vectors for Y_i and Y_j should either be the same or highly similar. By constructing a graph with connected nodes

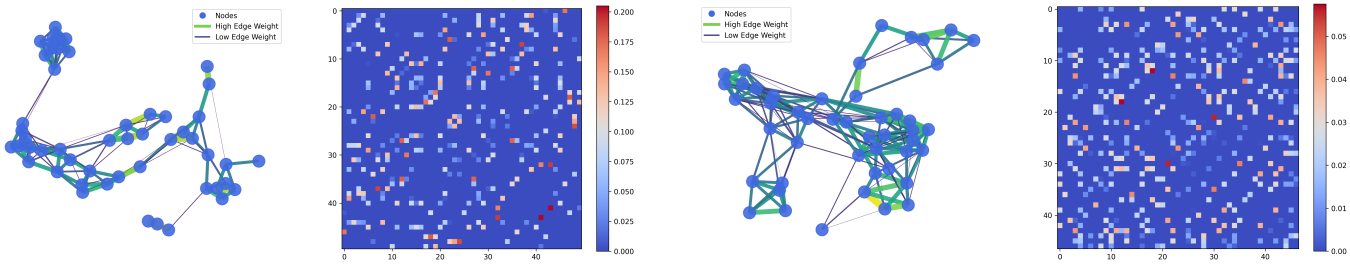

(a) Cylindrical model (b) Spherical model

Fig. 5: Visualization of the Gravity Graph for Cavity (GGFC) and corresponding edge heatmaps for (a) a cylindrical model and (b) a spherical model.

sharing feature similarities, the label information is propagated from labelled to unlabeled nodes based on proximity, assuming connected nodes have similar attributes and labels.

VI. Experiments

In this section, we present the experimental results of our proposed algorithms, GGFC-LapRLS and GGFC-GNN. We begin by conducting the homophily test, which validates the applicability of graph-based methods to cavity detection problems. Next, we assess the robustness of our approach in handling noisy data, assumed to be generated by the gravimeter and its surroundings. For benchmarking, we compare GGFC-LapRLS with Regularized Least Squares (RLS), and GGFC-GNN with Neural Networks (NN) [14], U-Net [34], and XGBoost (XGB) [59]. Finally, we evaluate our method on real gravimeter survey data for cavity detection and compare its performance with a previous Neural Network-based approach [14]. The source code is available at GGFC

A. Analysis of Cylindrical and Spherical Models

1) Dataset Generation: We generate gravity anomaly datasets containing 100, 500, 1000, 1500, 2000, 2500, and 10000 samples based on cylindrical and spherical subsurface structures using Table I. For each sample, the radius $R \sim \mathcal{U}(1.0, 4.0)$ m, depth to center $D \sim \mathcal{U}(2.0, 10.0)$ m, and density contrast $\Delta\rho \sim \mathcal{U}(-2500, -1500)$ kg/m^3 are drawn from uniform distributions over their respective ranges. Samples that violate the physical constraint $R < D/2$ are discarded to ensure realistic geometries. To simulate real-life measurement conditions, zero-mean Gaussian noise with a variance of 0.1 is added to the gravity anomaly values [60]. Each sample comprises 21 gravity anomaly readings measured at surface offsets uniformly spaced in the range $[-10, +10]$ m.

2) Homophily Analysis: We conducted experiments to validate the hypothesis that similarity cavities through stronger connections between nodes with similar features enhance the performance of graph-based cavity models. By applying the smoothness assumption over connected nodes, we expect that nodes with stronger weights will share similar labels. This guiding principle aims to improve the accuracy of predictions made by the graph-based cavity models.

1. Feature-based Graph of Cavities: A sparse graph and a heatmap Figure 5 describe the connections of the cavities. Global and Local homophily across different performance metrics validate the hypothesis shown in Table IV.

TABLE IV: Global and Local Node Label Assortativity Associated with Models Under Study

Feature based GGFC		
Test-Model	**Global**	**Local**
Cylindrical	0.52	0.55
Spherical	0.53	0.55

The graphs presented for both cylindrical and spherical models in Figure 5 provide strong empirical evidence supporting the hypothesis that nodes with similar features tend to share similar labels when they are connected within a graph. This finding underscores the potential of utilizing graph-based models to achieve accurate results in cavity detection.

3) Graph Learning: For the GGFC-LapRLS framework, a distance-based KNN method is used, where each node connects to its three nearest neighbors (K = 3). The edge weights are computed using an RBF kernel, and the resulting weighted adjacency matrix is used to derive the graph Laplacian (L).

For the GGFC-GNN framework, the graph structure is learned directly from the input features through a data-driven optimization process discussed in equation 3. Edge weights are initialized from a Gaussian distribution ($\mu = 0.5, \sigma = 0.01$), where μ denotes the mean and σ represents the standard deviation. The weights are updated over 5,000 iterations of projected gradient descent [61] with hyperparameters $\alpha = 1.0$, $\beta = 2.0$, and a learning rate $\eta = 0.001$. After convergence, only the top-weighted edges are retained to form a sparse adjacency matrix, preserving 5% of edges for GraphSAGE, 0.02% for GCN, and 0.1% for GAT.

4) Performance evaluation of GGFC-RLS and GGFC-GNN: After performing a homophilic test and verifying that the data is homophilic, the performance of the GGFC-LapRLS and GGFC-GNN models is evaluated using simulated training data generated from cylindrical and spherical models. Each dataset consists of 1000 samples, where the input data $X_i = f(\Delta g, \Delta\rho)$ and the corresponding labels Y_j represent cavity depth, making it a node-level regression problem.

Graphs are constructed using KNN for GGFC-LapRLS and graph learning via smoothness for GGFC-GNN. The dataset is initially split in an 80:20 ratio into training and testing sets. The testing set is further divided equally into validation

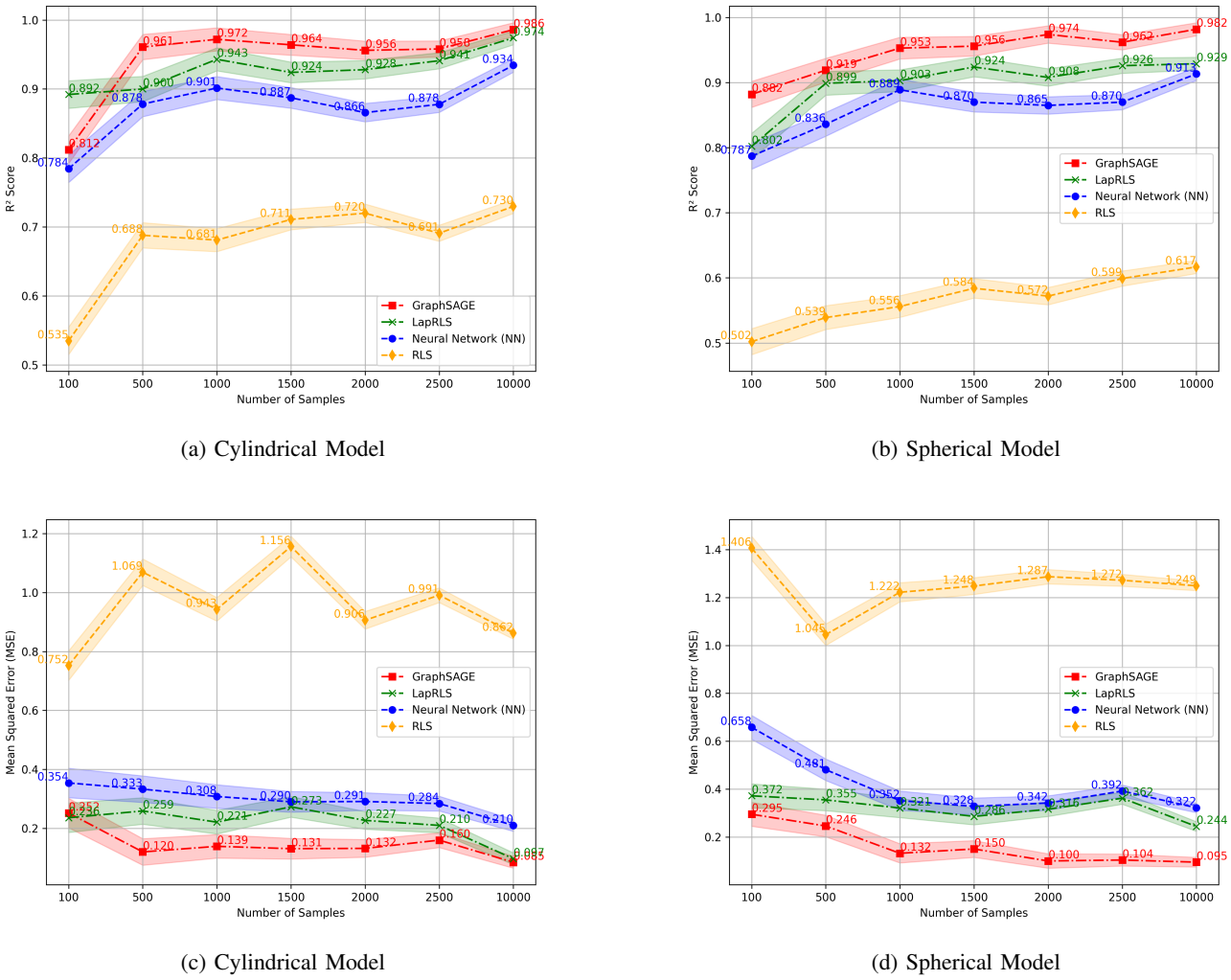

(a) Cylindrical Model

(b) Spherical Model

(c) Cylindrical Model

(d) Spherical Model

Fig. 6: (a, b) Variation of R^2-score and (c, d) Mean Squared Error (MSE) with different training sample sizes for the Cylindrical and Spherical models. All values are averaged over five runs.

TABLE V: R^2 scores with different methods across GGFC-GNN, GGFC-LapRLS, and traditional approaches using cylindrical and spherical models (Values shown are the mean and standard deviation, averaged across 5 runs)

Category	Method	Cylindrical Model	Spherical Model
GGFC-GNN	**SAGE**	$\mathbf{0.97 \pm 0.01}$	$\mathbf{0.95 \pm 0.01}$
	GCN	0.93 ± 0.01	0.90 ± 0.02
	GAT	0.93 ± 0.02	0.91 ± 0.01
GGFC-LapRLS	**LapRLS**	$\mathbf{0.94 \pm 0.02}$	$\mathbf{0.90 \pm 0.02}$
	RLS	0.68 ± 0.03	0.55 ± 0.03
Traditional	XGB [59]	0.90 ± 0.01	0.89 ± 0.01
	NN [14]	0.90 ± 0.02	0.88 ± 0.02
	LP [40]	0.60 ± 0.02	0.59 ± 0.02
	CG [28]	0.55 ± 0.01	0.57 ± 0.02

and final testing subsets. Model performance is evaluated using both the coefficient of determination (R^2) and the mean squared error (MSE) as evaluation metrics.

For GGFC-LapRLS, the model is benchmarked against the Regularised Least Squares (RLS) method, showing that incorporating graphs improves prediction accuracy. Similarly, for GGFC-GNN, GraphSAGE, Graph Convolutional Networks (GCN), and Graph Attention Networks (GAT) are evaluated and compared with a Neural Network (NN) baseline [14]. The connectivity of the graph is crucial for GNN performance in downstream tasks, as the node connections influence how well dependencies are captured and information is propagated [62]. As GraphSAGE outperforms other GNN and NN models and LapRLS performs better than RLS, we choose to compute the R^2 score and MSE on different labelled datasets, as shown in Figure 6. The results, presented in Tables V, show that both models benefit from graph integration. The performance metric is sensitive to the sparsity index. So varying the sparsity index significantly improves the performance of GCN and GAT. This improvement is reflected in the higher R^2 scores, which indicate a stronger correlation between the predicted and actual values, and thus a better overall fit to the data. For comparison with traditional methods, we use Laplace Propagation (LP) and the Conjugate Gradient (CG) approach, which demonstrate

significantly lower performance.

In this study, performance is influenced by the level of graph sparsity, which we tune individually for each architecture. We report the best-performing results for each method accordingly. Under this setting, GraphSAGE outperforms other architectures. While GAT and GCN also show strong performance, their results could vary with different sparsity configurations.

5) Impact of noise on model performance: This subsection evaluates the performance of our proposed method in noisy environments. Noise in gravimeter data measurement affects accuracy and precision, arising from electronic, mechanical, and temperature variations. Instrument noise, which remains relatively constant across locations, is primarily addressed during graph construction.

To assess robustness, we train the model with constant noise levels of 5%, 10%, and 20%, reflecting real-world variations. Additionally, we introduce Gaussian noise with zero mean and variances of 3%, 5%, and 8% to simulate practical noise intensities.

Despite noise interference, the model maintains strong performance for both cylindrical and spherical models. A higher R^2 score indicates resilience, as shown in Tables VI and VII.

TABLE VI: R^2 scores with different noise levels for both cylindrical and spherical models (Values shown are the mean and standard deviation, averaged across 5 runs)

Noise	(GGFC-LapRLS) R^2 Score	
	Cylindrical Model	Spherical Model
5%	0.94 ± 0.01	0.90 ± 0.01
10%	0.94 ± 0.02	0.90 ± 0.03
20%	0.94 ± 0.03	0.90 ± 0.03
3%-Gaussian	0.92 ± 0.02	0.86 ± 0.02
5%-Gaussian	0.89 ± 0.02	0.84 ± 0.03
8%-Gaussian	0.85 ± 0.03	0.82 ± 0.03

TABLE VII: R^2 scores with different noise levels for both cylindrical and spherical models (Values shown are the mean and standard deviation, averaged across 5 runs)

Noise	(GGFC-GNN) R^2 Score	
	Cylindrical Model	Spherical Model
5%	0.97 ± 0.01	0.95 ± 0.01
10%	0.97 ± 0.01	0.95 ± 0.01
20%	0.96 ± 0.01	0.94 ± 0.01
3%-Gaussian	0.95 ± 0.02	0.94 ± 0.03
5%-Gaussian	0.94 ± 0.02	0.89 ± 0.02
8%-Gaussian	0.92 ± 0.02	0.84 ± 0.03

B. Ablation Study

To evaluate the contribution of individual components in the GGFC-GNN's smooth signal-based graph learning framework, we conduct an ablation study by selectively removing regularisation terms from the original optimisation objective (Equation 3). The first term in the objective enforces smoothness via Dirichlet energy, the second term promotes graph connectivity, and the third term encourages sparsity. We assess the impact of each component using the R^2 score and MSE on both cylindrical and spherical cavity models.

a) Without Sparsity Constraint: We first examine the role of the sparsity-promoting ℓ_2 regularization term by removing it from the objective. This configuration evaluates the effect of sparsity enforcement on the learned graph structure. .

TABLE VIII: R^2 Score and MSE without sparsity constraint (Values shown are the mean and standard deviation, averaged across 5 runs).

Metric	Cylindrical Model	Spherical Model
R^2 Score	0.91 ± 0.01	0.92 ± 0.01
MSE	0.32 ± 0.05	0.26 ± 0.06

b) Without Connectivity Regularizer: Here, the connectivity-promoting regularisation term is removed to analyse its contribution to both the structural properties of the graph and predictive performance.

TABLE IX: R^2 Score and MSE without connectivity regularizer (Values shown are the mean and standard deviation, averaged across 5 runs).

Metric	Cylindrical Model	Spherical Model
R^2 Score	0.91 ± 0.01	0.90 ± 0.01
MSE	0.23 ± 0.02	0.20 ± 0.02

c) Without Connectivity and Sparsity (Pure Smoothness): Here, we retain only the Dirichlet energy term to isolate the effect of smooth signal learning without any regularization.

TABLE X: R^2 Score and MSE with only Dirichlet energy minimization (Values shown are the mean and standard deviation, averaged across 5 runs).

Metric	Cylindrical Model	Spherical Model
R^2 Score	0.90 ± 0.01	0.88 ± 0.02
MSE	0.31 ± 0.02	0.37 ± 0.02

d) Kernel Ablation Study: To assess the impact of the kernel function, we replace the RBF kernel in GGFC-LapRLS with a polynomial kernel. The results show a clear decline in performance, confirming the superiority of the RBF kernel for modeling complex gravitational features.

TABLE XI: R^2 Score and MSE for polynomial kernel (degree 3) (Values shown are the mean and standard deviation, averaged across 5 runs).

Metric	Cylindrical Model	Spherical Model
R^2 Score	0.91 ± 0.01	0.85 ± 0.02
MSE	0.28 ± 0.05	0.58 ± 0.12

e) KNN Graph Construction with GraphSAGE: We explore the effect of using a K-nearest neighbors (KNN) graph in combination with GraphSAGE for feature aggregation. This configuration improves local structural learning and enhances depth estimation accuracy.

TABLE XII: R^2 Score and MSE for GraphSAGE using KNN graph (Values shown are the mean and standard deviation, averaged across 5 runs).

Metric	Cylindrical Model	Spherical Model
R^2 Score	0.96 ± 0.01	0.95 ± 0.01
MSE	0.15 ± 0.02	0.14 ± 0.01

f) Smooth Signal Learning with LapRLS: Finally, we evaluate the use of Laplacian Regularized Least Squares (LapRLS) to enforce smoothness in the label space. The results affirm the importance of leveraging graph structure for accurate cavity depth estimation.

TABLE XIII: R^2 Score and MSE for LapRLS using smooth signal learning (Values shown are the mean and standard deviation, averaged across 5 runs).

Metric	Cylindrical Model	Spherical Model
R^2 Score	0.92 ± 0.01	0.89 ± 0.01
MSE	0.28 ± 0.02	0.37 ± 0.04

These ablation results collectively highlight the significance of each regularization component, kernel selection, and graph construction strategy in the performance of our proposed GGFC-GNN framework.

C. Factors Affecting Radius Accuracy

In the context of error propagation, the radius depends on the depth—predicted by models such as GGFC-GNN and GGFC-RLS—as well as on the gravity anomaly (Δg) and the density contrast ($\Delta \rho$). While Δg is directly measured using a gravimeter and $\Delta \rho$ is typically assumed based on geological estimates (since the cavity density is known in this problem), the depth must often be inferred through model predictions. As a result, uncertainties in all three variables—predicted depth, measured gravity anomaly, and assumed density contrast—contribute to the overall error in radius estimation.

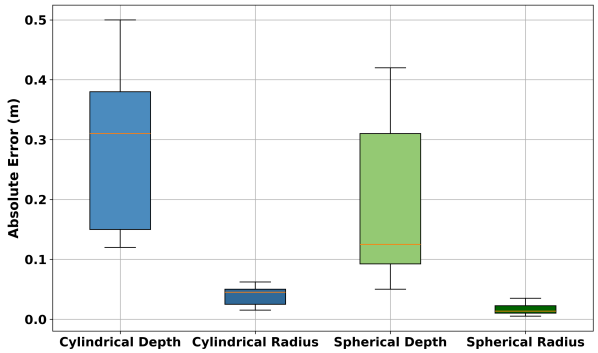

Fig. 7: Box plot showing depth and radius absolute errors for cylindrical and spherical models.

The box plot illustrates the absolute errors in depth and radius estimation for cylindrical and spherical models. It reveals that depth errors are notably higher and more variable than radius errors in both geometries. Specifically, the cylindrical depth error shows the largest spread and median, indicating greater inconsistency, while the spherical radius error is the most compact and lowest, reflecting high accuracy and stability. This comparison emphasises that radius predictions are consistently reliable, whereas depth estimation remains a more challenging task, especially for cylindrical shapes.

D. Model Robustness to Resolution and Density Fluctuations

To simulate a small density contrast in the subsurface, we model two buried bodies—a larger outer body and a smaller inner body with different shapes (cylindrical or spherical) and densities. The outer body has a density of $1800\ \mathrm{kg/m^3}$, while the inner cavity has a lower density of $-1500\ \mathrm{kg/m^3}$, representing a void or low-density region surrounded by denser material. Based on this setup, we generate gravitational anomaly data. We create 1000 samples by randomly varying the depths and radii of the bodies, with depths ranging from 2.0 to 10.0 m and radii ranging from 1.0 to 4.0 m. We also apply geometric constraints to ensure that both bodies remain fully buried and that the outer body is always larger than the inner one. We compute gravitational anomalies at 21 surface positions for each configuration and add Gaussian noise to simulate real-world measurement conditions. This data is then used to evaluate the performance of our two models, GGFC-GNN and GGFC-RLS, with the results summarised in the following table.

TABLE XIV: Performance metrics with Density constraint.

Metric	Cylindrical Model	Spherical Model
R^2 Score	$0.94\pm$ 0.01	0.92 ± 0.01
MSE	0.14 ± 0.01	0.15 ± 0.01

The results demonstrate the effectiveness of our method in scenarios with low density contrast.

E. Analysis of Irregular Models

In this experiment, we evaluate the performance of a GraphSAGE-based Graph Neural Network (GGFC-GNN) for detecting irregular subsurface cavities from gravity anomaly data. The dataset consists of 2500 samples, with 22 input features per sample and 252 binary output labels representing discretized subsurface blocks. The GNN model employs four SAGEConv layers with dropout, and training uses Dice loss for binary classification. Early stopping with patience is applied to prevent overfitting, and results are aggregated over five random seeds to assess robustness. Model performance is evaluated using standard metrics, including F1-score, and Jaccard Index/Intersection of Union (IoU).

While the Intersection over Union (IoU) metric evaluates the spatial overlap between the predicted cavities and the ground truth, the F1-score emphasizes the model's ability to balance false positives and false negatives. Together, these metrics provide a comprehensive assessment of both localization and classification performance. For evaluation, we compare our method against a UNet-based deep learning approach with Dice loss for 3D sparse inversion of gravity data as a baseline. The results of this comparison are presented in Table XV.

The results in Figure 8, and Figure 9 demonstrate the robustness of the proposed framework in addressing datasets

Method	IoU	F1-Score
GGFC-GNN	$\mathbf{0.84 \pm 0.01}$	$\mathbf{0.61 \pm 0.01}$
UNet [34]	0.79 ± 0.01	0.59 ± 0.01

TABLE XV: Performance comparison of GGFC-GNN and UNet

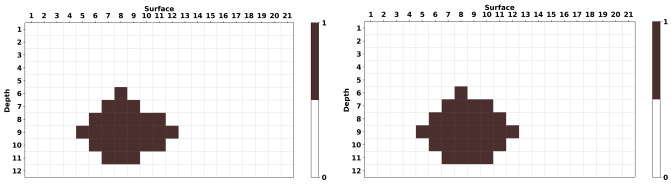

(a) True (b) Predicted

Fig. 8: Comparison of the true cavity model (left) and the predicted cavity model (right) for Irregular Models using GGFC-GNN.

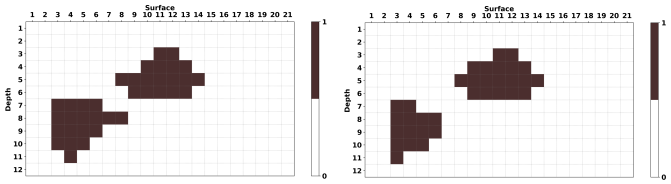

(a) True (b) Predicted

Fig. 9: Comparison of the true multi-cavity model (left) and the predicted model (right) for irregular and spatially separated cavities.

with Irregular Models, encompassing both single and multiple cavities. These findings confirm that the extended framework is adaptable and applicable to a broad spectrum of practical scenarios.

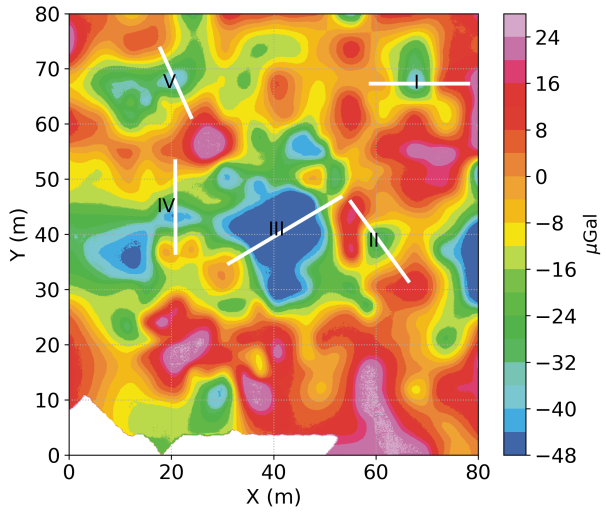

Fig. 10: Residual gravity anomaly map of the Medford Cave Site [63], highlighting the locations of five selected profiles used as real-data test examples.

Our method estimates the cavity centre and radius by identifying depth ranges from the cavity's top to bottom, consistently locating the centre within the cavity. However, as all methods are designed for single-cavity detection, none accurately identify profile III due to its multi-cavity structure.

Figure 11 shows the absolute error between predicted cavity centers and borehole-derived centers, demonstrating minimal deviations. Additionally, our method captures the cylindrical nature of Medford Cave and aligns well with real-world observations. Overall, extensive experiments confirm the effectiveness of graph-based semi-supervised learning methods in geoscientific applications.

TABLE XVI: Borehole coordinates (X,Y), density contrasts $\Delta\rho$, and per-profile offsets.

Profile	X (m)	Y (m)	$\Delta\rho$ (kg m^{-3})	Offset (m)
I	54.86	67.06	-1660	3.28
II	60.96	39.62	-1680	0.41
III	54.86	36.58	-1720	5.74
IV	32.61	49.38	-1850	11.61
V	33.53	57.91	-1050	10.01

F. Real-World Application and Validation

In Butler's studies from 1983 [63] and 1984 [12], a microgravity survey was conducted at the Medford Cave site using a LaCoste-Romberg model D-4 gravimeter. A total of 420 readings were collected over an 80 m × 80 m area, with a grid spacing of 6.1 m (20 ft) and a finer 3 m (10 ft) grid over the central cavity system. Standard corrections, including tidal, drift, Bouguer, and terrain corrections, were applied.

To assess the accuracy of cavity detection, five profile lines (I–V), shown in Figure 10, are selected across gravity anomalies and positioned near boreholes for validation [63].

Table XVI summarizes the borehole coordinates, density contrasts, and per-profile offsets. Profiles I, II, IV, and V were used in the MAE calculations, as they are located near the main negative gravity anomaly. The density contrasts ($\Delta\rho$) range from -1000 to -1900 kg m^{-3}. The offset values for each profile are also presented. For the preprocessing stage, the discrete data were interpolated using a geostatistical Kriging [64] interpolation scheme, and resampling was done at 1 m spatial spacing. The resulting gravity anomaly is expressed in microgals (μGal).

Tables XVII–XX present the estimated parameters for these profiles based on cylindrical and spherical cavity models. We compare the results of our graph-based LapRLS and GNN methods with those from a previously developed neural network approach and corresponding borehole data [14]. Figure 12 presents the visualization of five profiles obtained using GGFC-GNN for irregularly shaped cavities, where Profiles I, II, IV, and V correspond to single cavities, while Profile III represents a multicavity case. The visualizations further confirm that the detected cavities lie within the verified range.

VII. Limitation

Our framework is specifically designed for microgravity surveys focused on detecting shallow subsurface cavities, and its applicability to large-scale or deeper structures remains limited. This limitation suggests an important direction for

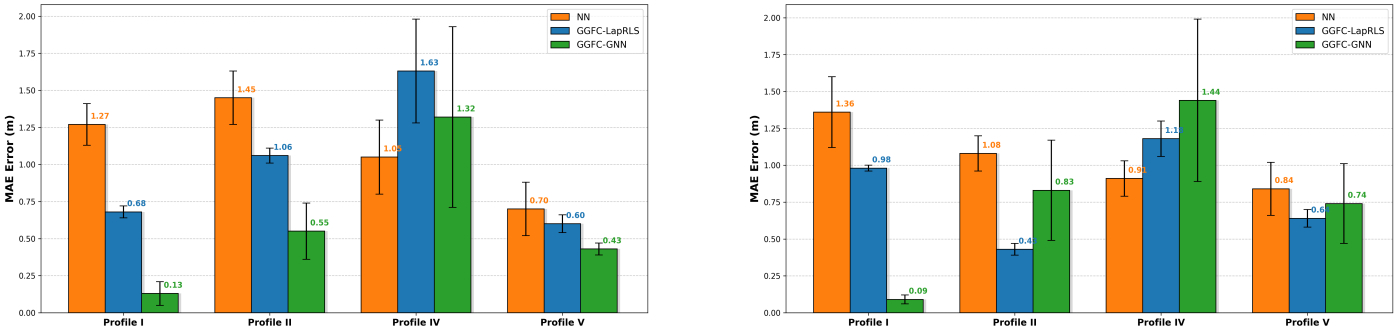

(a) Cylindrical model (b) Spherical model

Fig. 11: Comparison of Mean Absolute Error (MAE) and Standard Deviation in depth prediction for the Medford cave profiles using (a) Cylindrical and (b) Spherical models.

TABLE XVII: **Cylindrical Model in GGFC-LapRLS:** The method defines 'T' as the top, 'B' as the bottom, 'D' as the center, and 'R' as the cavity radius, with all measurements in meters (averaged over five runs).

Anomaly No.	Neural Network				GGFC-LapRLS				Boring Depth			
	T(m)	*B(m)*	*D(m)*	*R(m)*	*T(m)*	*B(m)*	*D(m)*	*R(m)*	*T(m)*	*B(m)*	*D(m)*	*R(m)*
Profile I	3.19	6.13	4.84	1.65	2.70	5.80	4.25	1.55	2.74	4.41	3.57	0.84
Profile II	3.92	7.20	5.56	1.64	2.47	6.76	5.17	1.59	2.74	5.48	4.11	1.37
Profile IV	2.85	6.11	4.80	1.63	2.61	5.75	4.22	1.53	3.90	7.80	5.85	1.90
Profile V	2.67	6.85	4.76	2.09	1.68	5.24	3.46	1.78	2.71	5.42	4.06	1.36

TABLE XVIII: **Spherical Model in GGFC-LapRLS:** The method defines 'T' as the top, 'B' as the bottom, 'D' as the center, and 'R' as the cavity radius, with all measurements in meters (averaged over five runs).

Anomaly No.	Neural Network				GGFC-LapRLS				Boring Depth			
	T(m)	*B(m)*	*D(m)*	*R(m)*	*T(m)*	*B(m)*	*D(m)*	*R(m)*	*T(m)*	*B(m)*	*D(m)*	*R(m)*
Profile I	2.19	6.67	4.93	2.74	1.95	7.15	4.55	2.60	2.74	4.41	3.57	0.84
Profile II	2.49	7.89	5.19	2.70	2.07	7.01	4.54	2.47	2.74	5.48	4.11	1.37
Profile IV	2.22	7.66	4.94	2.72	2.05	7.29	4.67	2.62	3.90	7.80	5.85	1.90
Profile V	1.69	8.11	4.90	3.21	0.89	5.95	3.42	2.53	2.71	5.42	4.06	1.36

TABLE XIX: **Cylindrical Model in GGFC-GNN:** The method defines 'T' as the top, 'B' as the bottom, 'D' as the center, and 'R' as the cavity radius, with all measurements in meters (averaged over five runs).

Anomaly No.	Neural Network				GGFC-GNN				Boring Depth			
	T(m)	*B(m)*	*D(m)*	*R(m)*	*T(m)*	*B(m)*	*D(m)*	*R(m)*	*T(m)*	*B(m)*	*D(m)*	*R(m)*
Profile I	3.19	6.13	4.84	1.65	2.05	4.83	3.44	1.39	2.74	4.41	3.57	0.84
Profile II	3.92	7.20	5.56	1.64	2.25	4.87	3.56	1.31	2.74	5.48	4.11	1.37
Profile IV	2.85	6.11	4.80	1.63	2.95	6.11	4.53	1.58	3.90	7.80	5.85	1.90
Profile V	2.67	6.85	4.76	2.09	1.80	5.46	3.63	1.83	2.71	5.42	4.06	1.36

TABLE XX: **Spherical Model in GGFC-GNN:** The method defines 'T' as the top, 'B' as the bottom, 'D' as the center, and 'R' as the cavity radius, with all measurements in meters (averaged over five runs).

Anomaly No.	Neural Network				GGFC-GNN				Boring Depth			
	T(m)	*B(m)*	*D(m)*	*R(m)*	*T(m)*	*B(m)*	*D(m)*	*R(m)*	*T(m)*	*B(m)*	*D(m)*	*R(m)*
Profile I	2.19	6.67	4.93	2.74	1.31	5.64	3.48	2.17	2.74	4.41	3.57	0.84
Profile II	2.49	7.89	5.19	2.70	1.29	5.27	3.28	1.99	2.74	5.48	4.11	1.37
Profile IV	2.22	7.66	4.94	2.72	1.89	6.93	4.41	2.52	3.90	7.80	5.85	1.90
Profile V	1.69	8.11	4.90	3.21	0.84	5.6	3.32	2.48	2.71	5.42	4.06	1.36

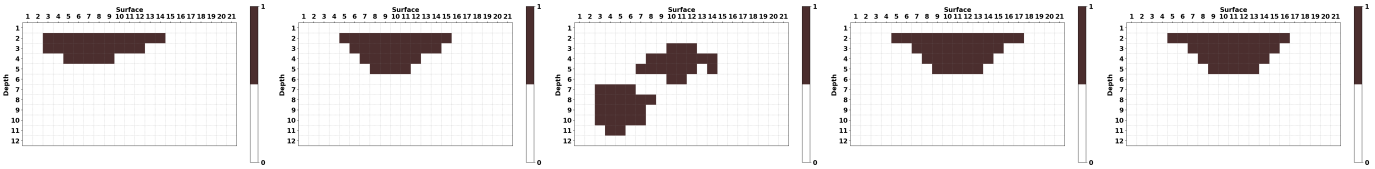

(a) Profile I (b) Profile II (c) Profile III (d) Profile IV (e) Profile V

Fig. 12: Visualization of five profiles from the Medford Cave dataset, where the shaded regions denote cavities and the white regions represent the background.

TABLE XXI: Profile III (Multi-Cavity) Results: The profile represents a multicavity case, and our models accurately predict the entire range of the cavity structure. The method defines 'T' as the top, 'B' as the bottom, 'D' as the center, and 'R' as the cavity radius, with all measurements in meters (averaged over five runs).

Model Type	Method	*T(m)*	*B(m)*	*D(m)*	*R(m)*
Cylindrical	Neural Network	5.48	11.14	8.31	2.83
	GGFC-LapRLS	5.41	11.05	8.23	2.82
	GGFC-GNN	5.68	11.42	8.55	2.87
	Boring Depth	4.57	7.92	6.25	1.68
		8.68	9.29	8.98	0.31
Spherical	Neural Network	1.94	8.92	5.34	3.49
	GGFC-LapRLS	2.09	9.31	5.70	3.61
	GGFC-GNN	3.28	12.08	7.68	4.40
	Boring Depth	4.57	7.92	6.25	1.68
		8.68	9.29	8.98	0.31

future research by extending the GGFC-LapRLS and GGFC-GNN frameworks to broader survey ranges and large-scale geological applications.

VIII. Conclusion

In this paper, we developed two graph-based methods, GGFC-LapRLS and GGFC-GNN, for cavity detection from gravity data in microgravity surveys. Both approaches leverage spatial relationships and cavity similarities to improve detection accuracy, with GGFC-GNN achieving higher performance and GGFC-LapRLS offering lower complexity and faster training. Our validation on gravity data from the Medford Cave site using cylindrical and spherical cavity models demonstrates that both methods can effectively predict cavity specifications at depths ranging from 1 to 12 meters. Cylindrical and spherical models, in particular, find applications in representing subsurface voids such as pipelines and storage tanks. To extend beyond regular geometries, we further developed an extension of GGFC-GNN capable of detecting irregularly shaped cavities, thereby enhancing the practical utility of our framework in realistic geological settings where cavity boundaries deviate from idealized forms. Moreover, our methods remain robust under noisy conditions, highlighting their reliability and efficiency for real-world subsurface exploration. Taken together, these contributions establish a foundation for accurate and computationally efficient cavity detection across a broad spectrum of geological and engineering applications.

References

[1] A. G. Camacho, F. G. Montesinos, and R. Vieira, "Gravity inversion by means of growing bodies," *Geophysics*, vol. 65, no. 1, pp. 95–101, 2000.

[2] Y. Bidel, O. Carraz, R. Charrière, M. Cadoret, N. Zahzam, and A. Bresson, "Compact cold atom gravimeter for field applications," *Applied Physics Letters*, vol. 102, no. 14, 2013.

[3] P. Styles, R. McGrath, E. Thomas, and N. Cassidy, "The use of microgravity for cavity characterization in karstic terrains," *Quarterly Journal of Engineering Geology and Hydrogeology*, vol. 38, no. 2, pp. 155–169, 2005.

[4] S. Adams, "Gas saturation monitoring in north oman reservoir using a borehole gravimeter," in *Middle East Oil Show*. OnePetro, 1991.

[5] Q. Guan, S. Ren, L. Chen, Y. Yao, Y. Hu, R. Wang, B. Feng, L. Gu, and W. Chen, "Recognizing multivariate geochemical anomalies related to mineralization by using deep unsupervised graph learning," *Natural Resources Research*, vol. 31, no. 5, pp. 2225–2245, 2022.

[6] M. Ukawa, K. Nozaki, H. Ueda, and E. Fujita, "Calibration shifts in scintrex cg-3m gravimeters with an application to detection of microgravity changes at iwo-tou caldera, japan," *Geophysical prospecting*, vol. 58, no. 6, pp. 1123–1132, 2010.

[7] W. Freeden and M. Zuhair Nashed, "Inverse gravimetry as an ill-posed problem in mathematical geodesy," in *Handbook of Mathematical Geodesy: Functional Analytic and Potential Theoretic Methods*. Springer, 2018, pp. 641–685.

[8] Y. Li and D. W. Oldenburg, "3-d inversion of magnetic data," *Geophysics*, vol. 61, no. 2, pp. 394–408, 1996.

[9] D. K. Butler, "Detection and characterization of subsurface cavities, tunnels and abandoned mines," *Near-surface geophysics and human activity*, pp. 578–584, 2008.

[10] Y. Fang, J. Wang, Z. Zhou, F. Li, X. Meng, and S. Zheng, "Improved 3-d joint inversion of gravity and magnetic data based on deep learning with a multi-task learning strategy," *IEEE Transactions on Geoscience and Remote Sensing*, vol. 63, no. 7, pp. 3401–3415, Jul 2025.

[11] R. Wang, Y. Ding, Z. Xu, M. S. Zhdanov, M. Xian, Y. Zhang, J. Li, C. Jiang, and Z. Guo, "Employing ms-unets networks for multiscale 3d gravity data inversion: A case study in the nordkapp basin, barents sea," *IEEE Transactions on Geoscience and Remote Sensing*, 2024.

[12] D. K. Butler, "Microgravimetric and gravity gradient techniques for detection of subsurface cavities," *Geophysics*, vol. 49, no. 7, pp. 1084–1096, 1984.

[13] D. McCann, P. Jackson, and M. Culshaw, "The use of geophysical surveying methods in the detection of natural cavities and mineshafts," *Quarterly Journal of Engineering Geology*, vol. 20, no. 1, pp. 59–73, 1987.

[14] K. U. E. Elawadi, A. Salem, "Detection of cavities and tunnels from gravity data using a neural network," *Exploration Geophysics*, vol. 32, no. 3-4, pp. 204–208, 2001.

[15] G. Tuckwell, T. Grossey, S. Owen, and P. Stearns, "The use of microgravity to detect small distributed voids and low-density ground," *Quarterly Journal of Engineering Geology and Hydrogeology*, vol. 41, no. 3, pp. 371–380, 2008.

[16] S. Porzucek and M. Loj, "Microgravity survey to detect voids and loosening zones in the vicinity of the mine shaft," *Energies*, vol. 14, no. 11, p. 3021, 2021.

[17] R. J. Chico, "Detection of caves by gravimetry," *International Journal of Speleology*, vol. 1, no. 1, p. 11, 1964.

[18] J. Munk and R. A. Sheets, *Detection of underground voids in Ohio by use of geophysical methods*. US Department of the Interior, US Geological Survey, 1997, vol. 97, no. 4221.

[19] I. Bishop, P. Styles, S. Emsley, and N. Ferguson, "The detection of cavities using the microgravity technique: case histories from mining and karstic environments," *Geological Society, London, Engineering Geology Special Publications*, vol. 12, no. 1, pp. 153–166, 1997.

[20] A. T. H. Ibrahim and C. N. Lat, "Detecting subsurface voids using the microgravity method–a case study from kuala lipis, pahang," 2004.

[21] W. Lowrie and A. Fichtner, *Fundamentals of geophysics*. Cambridge university press, 2020.

[22] M. El-Tokhey, M. Elhabiby, A. Ragheb, and M. Shebl, "Gravity and density relationship (forward modelling)," *International Journal of Scientific & Engineering Research*, vol. 6, no. 1, 2015.

[23] A. Arisona, K. Ishola, M. Muliddin, L. Hamimu, and H. Hasria, "The potential of microgravity technique in subsurface cavities detection at chan sow lin site in kuala lumpur, malaysia: a case study," *Modeling Earth Systems and Environment*, vol. 9, no. 1, pp. 771–782, 2023.

[24] L. Misici and F. Zirilli, "The inverse gravimetry problem: an application to the northern san francisco craton granite," *Journal of optimization theory and applications*, vol. 63, no. 1, pp. 39–49, 1989.

[25] J. B. C. Silva, W. E. Medeiros, and V. C. F. Barbosa, "Potential-field inversion: Choosing the appropriate technique to solve a geologic problem," *Geophysics*, vol. 66, no. 2, pp. 511–520, 2001.

[26] Y. Li and D. W. Oldenburg, "3-d inversion of gravity data," *Geophysics*, vol. 63, no. 1, pp. 109–119, Jan 1998.

[27] M. Fedi and A. Rapolla, "3-d inversion of gravity and magnetic data with depth resolution," *Geophysics*, vol. 64, no. 2, pp. 452–460, Mar 1999.

[28] M. R. Hestenes, "Conjugate direction methods in optimization," in *Optimization Techniques Part 1: Proceedings of the 8th IFIP Conference on Optimization Techniques Würzburg, September 5–9, 1977*. Springer, 2005, pp. 8–27.

[29] M. S. Frank and C. A. Balanis, "A conjugate direction method for geophysical inversion problems," *IEEE Transactions on Geoscience and Remote Sensing*, no. 6, pp. 691–701, 1987.

[30] J. Adler and O. Öktem, "Solving ill-posed inverse problems using iterative deep neural networks," *Inverse Problems*, vol. 33, no. 12, p. 124007, 2017.

[31] A. Karpatne, I. Ebert-Uphoff, S. Ravela, H. A. Babaie, and V. Kumar, "Machine learning for the geosciences: Challenges and opportunities," *IEEE Transactions on Knowledge and Data Engineering*, vol. 31, no. 8, pp. 1544–1554, 2018.

[32] Q. Yang, X. Hu, S. Liu, Q. Jie, H. Wang, and Q. Chen, "3-d gravity inversion based on deep convolution neural networks," *IEEE geoscience and remote sensing letters*, vol. 19, pp. 1–5, 2021.

[33] W. Yu-Feng, Z. Yu-Jie, F. Li-Hua, and L. Hong-Wei, "Three-dimensional gravity inversion based on 3d u-net++," *Applied Geophysics*, vol. 18, no. 4, pp. 451–460, 2021.

[34] R. Huang, S. Liu, R. Qi, and Y. Zhang, "Deep learning 3d sparse inversion of gravity data," *Journal of Geophysical Research: Solid Earth*, vol. 126, no. 11, p. e2021JB022476, 2021.

[35] S. He, H. Cai, S. Liu, J. Xie, and X. Hu, "Recovering 3d basement relief using gravity data through convolutional neural networks," *Journal of Geophysical Research: Solid Earth*, vol. 126, no. 10, p. e2021JB022611, 2021.

[36] S. Zhang, C. Yin, X. Cao, S. Sun, Y. Liu, and X. Ren, "Decnet: Decomposition network for 3d gravity inversion," *Geophysics*, vol. 87, no. 5, pp. G103–G114, 2022.

[37] S. Dong, J. Jiao, S. Zhou, P. Lu, and Z. Zeng, "3-d gravity data inversion based on enhanced dual u-net framework," *IEEE Transactions on Geoscience and Remote Sensing*, 2023.

[38] S. Kumar, J. Ying, J. V. d. M. Cardoso, and D. P. Palomar, "A unified framework for structured graph learning via spectral constraints," *Journal of Machine Learning Research*, vol. 21, no. 22, pp. 1–60, 2020.

[39] F. Xia, K. Sun, S. Yu, A. Aziz, L. Wan, S. Pan, and H. Liu, "Graph learning: A survey," *IEEE Transactions on Artificial Intelligence*, vol. 2, no. 2, pp. 109–127, 2021.

[40] X. Zhu and Z. Ghahramani, "Learning from labeled and unlabeled data with label propagation," *Technical Report CMU-CALD-02-107, Carnegie Mellon University*, 2002.

[41] X. Jia, S. Chen, C. Zheng, Y. Xie, Z. Jiang, and N. Kalanat, "Physics-guided graph diffusion network for combining heterogeneous simulated data: An application in predicting stream water temperature," in *Proceedings of the 2023 SIAM International Conference on Data Mining (SDM)*. SIAM, 2023, pp. 361–369.

[42] H. Farahmand, Y. Xu, and A. Mostafavi, "A spatial–temporal graph deep learning model for urban flood nowcasting leveraging heterogeneous community features," *Scientific Reports*, vol. 13, no. 1, p. 6768, 2023.

[43] F.-H. Zhang and Z.-G. Shao, "St-grf: Spatiotemporal graph neural networks for rainfall forecasting," *Digital Signal Processing*, vol. 136, p. 103989, 2023.

[44] Z. Ma, G. Mei, S. Cuomo, and F. Piccialli, "Heterogeneous data fusion considering spatial correlations using graph convolutional networks and its application in air quality prediction," *Journal of King Saud University-Computer and Information Sciences*, vol. 34, no. 6, pp. 3433–3447, 2022.

[45] T. Owen, "Detection and mapping of tunnels and caves," *Developments, in Geophysical Exploration Methods*, vol. 5, pp. 161–258, 1983.

[46] J. Cohen, E. Rosenfeld, and Z. Kolter, "Certified adversarial robustness via randomized smoothing," in *international conference on machine learning*. PMLR, 2019, pp. 1310–1320.

[47] W. Dong, C. Moses, and K. Li, "Efficient k-nearest neighbor graph construction for generic similarity measures," in *Proceedings of the 20th international conference on World wide web*, 2011, pp. 577–586.

[48] V. Kalofolias, "How to learn a graph from smooth signals," in *Artificial intelligence and statistics*. PMLR, 2016, pp. 920–929.

[49] K. Zhou, X. Huang, D. Zha, R. Chen, L. Li, S.-H. Choi, and X. Hu, "Dirichlet energy constrained learning for deep graph neural networks," *Advances in Neural Information Processing Systems*, vol. 34, pp. 21 834–21 846, 2021.

[50] M. Belkin, P. Niyogi, and V. Sindhwani, "Manifold regularization: A geometric framework for learning from labeled and unlabeled examples." *Journal of machine learning research*, vol. 7, no. 11, 2006.

[51] T. N. Kipf and M. Welling, "Semi-supervised classification with graph convolutional networks," *arXiv preprint arXiv:1609.02907*, 2016.

[52] W. Hamilton, Z. Ying, and J. Leskovec, "Inductive representation learning on large graphs," *Advances in neural information processing systems*, vol. 30, 2017.

[53] P. Velickovic, G. Cucurull, A. Casanova, A. Romero, P. Lio, Y. Bengio *et al.*, "Graph attention networks," *stat*, vol. 1050, no. 20, pp. 10–48 550, 2017.

[54] O. Boulanger and M. Chouteau, "Constraints in 3d gravity inversion," *Geophysical prospecting*, vol. 49, no. 2, pp. 265–280, 2001.

[55] J. Zhu, Y. Yan, L. Zhao, M. Heimann, L. Akoglu, and D. Koutra, "Beyond homophily in graph neural networks: Current limitations and effective designs," *Advances in neural information processing systems*, vol. 33, pp. 7793–7804, 2020.

[56] Y. Hou, J. Zhang, J. Cheng, K. Ma, R. T. B. Ma, H. Chen, and M.-C. Yang, "Measuring and improving the use of graph information in graph neural networks," 2022.

[57] M. E. Newman, "Mixing patterns in networks," *Physical review E*, vol. 67, no. 2, p. 026126, 2003.

[58] Y. Li, B. Lin, B. Luo, and N. Gui, "Graph representation learning beyond node and homophily," *IEEE Transactions on Knowledge and Data Engineering*, vol. 35, no. 5, pp. 4880–4893, 2022.

[59] T. Chen and C. Guestrin, "Xgboost: A scalable tree boosting system," in *Proceedings of the 22nd acm sigkdd international conference on knowledge discovery and data mining*, 2016, pp. 785–794.

[60] S. Rosat and J. Hinderer, "Limits of detection of gravimetric signals on earth," *Scientific Reports*, vol. 8, no. 1, p. 15324, 2018.

[61] S. Boyd and L. Vandenberghe, *Convex optimization*. Cambridge university press, 2004.

[62] J. Zhou, G. Cui, S. Hu, Z. Zhang, C. Yang, Z. Liu, L. Wang, C. Li, and M. Sun, "Graph neural networks: A review of methods and applications," *AI open*, vol. 1, pp. 57–81, 2020.

[63] D. K. Butler and G. L. (US), *Cavity Detection and Delineation Research: Report 1: Microgravimetric and Magnetic Surveys: Medford Cave Site, Florida*. Geotechnical Laboratory, US Army Engineer Waterways Experiment Station, 1983.

[64] J.-P. Chilès and N. Desassis, "Fifty years of kriging," in *Handbook of mathematical geosciences: Fifty years of IAMG*. Springer International Publishing Cham, 2018, pp. 589–612.

Gourab Panda received his M.E. degree from Jadavpur University, Kolkata, India. He is currently pursuing the Ph.D. degree with the Indian Institute of Technology Delhi, New Delhi, India. His research interests include graph machine learning, artificial intelligence for geoscience applications, gravity data inversion, subsurface imaging, image processing, and optimization.

Vipul Kumar Singh (Student Member, IEEE) received his M.Tech. degree from the Indian Institute of Technology, Patna, India. He is currently pursuing a Ph.D. degree at the Indian Institute of Technology, Delhi, India. He is a recipient of the Prime Minister's Research Fellowship. His research interests include graph machine learning, trustworthy machine learning, biomedical signal and image processing, and optimization.

Anil Kumar received the Ph.D. degree through a joint doctoral program between Monash University, Australia, and the Indian Institute of Technology Bombay, India, and the B.Tech. degree from the Indian Institute of Technology Roorkee, India. He is currently a Principal Project Scientist with the Indian Institute of Technology Delhi, India. His research interests include geophysical inversion, reduced-order modeling, physics-informed machine learning, and AI-driven surrogate modeling for large-scale subsurface and environmental systems.

Manabendra Saharia is an Associate Professor of the Department of Civil and Environmental Engineering and Associate Faculty at the Yardi School of Artificial Intelligence at Indian Institute of Technology Delhi. Previously with NASA and NCAR, he currently leads the HydroSense Lab and the Center of Excellence on Water at IIT Delhi. He earned his Ph.D. in Water Resources Engineering from the University of Oklahoma/National Weather Center. His research integrates Geospatial AI, hydrologic modeling and multi-sensor remote sensing to advance flood and landslide forecasting, and the development of operational, decision-centric digital twins. Dr. Saharia's scientific contributions have been recognized with the Young Scientist Award from the The National Academy of Sciences India (NASI) and the Indian National Geospatial Award.

Sandeep Kumar is an associate professor in the Department of Electrical Engineering, Yardi School of Artificial Intelligence, an associate faculty at Bharti School of Telecommunication Technology and Management at the Indian Institute of Technology Delhi (IIT Delhi), and is honored with the DST Inspire Faculty Fellowship Award and the TCS Doctoral Fellowship. At IIT Delhi, he leads the Machine Intelligence Signals and Networks (MISN) lab. His research explores the intersection of machine learning, graphical models, and deep learning, addressing complex data challenges.